



# Stabilization of ammonia-rich hydrate inside icy planets

Victor Naden Robinson<sup>a,b</sup>, Yanchao Wang<sup>c</sup>, Yanming Ma<sup>c,d</sup>, and Andreas Hermann<sup>a,b,1</sup>

<sup>a</sup>Centre for Science at Extreme Conditions, School of Physics and Astronomy, The University of Edinburgh, Edinburgh, EH9 3FD, United Kingdom; <sup>b</sup>Scottish Universities Physics Alliance, School of Physics and Astronomy, The University of Edinburgh, Edinburgh, EH9 3FD, United Kingdom; <sup>c</sup>State Key Laboratory of Superhard Materials, College of Physics, Jilin University, Changchun 130012, China; and <sup>d</sup>International Center for Future Science, Jilin University, Changchun 130012, China

Edited by Russell J. Hemley, The George Washington University, Washington, DC, and approved July 11, 2017 (received for review April 14, 2017)

**The interior structure of the giant ice planets Uranus and Neptune, but also of newly discovered exoplanets, is loosely constrained, because limited observational data can be satisfied with various interior models. Although it is known that their mantles comprise large amounts of water, ammonia, and methane ices, it is unclear how these organize themselves within the planets—as homogeneous mixtures, with continuous concentration gradients, or as well-separated layers of specific composition. While individual ices have been studied in great detail under pressure, the properties of their mixtures are much less explored. We show here, using first-principles calculations, that the 2:1 ammonia hydrate, (H<sub>2</sub>O)(NH<sub>3</sub>)<sub>2</sub>, is stabilized at icy planet mantle conditions due to a remarkable structural evolution. Above 65 GPa, we predict it will transform from a hydrogen-bonded molecular solid into a fully ionic phase O<sup>2-</sup>(NH<sub>4</sub><sup>+</sup>)<sub>2</sub>, where all water molecules are completely deprotonated, an unexpected bonding phenomenon not seen before. Ammonia hemihydrate is stable in a sequence of ionic phases up to 500 GPa, pressures found deep within Neptune-like planets, and thus at higher pressures than any other ammonia–water mixture. This suggests it precipitates out of any ammonia–water mixture at sufficiently high pressures and thus forms an important component of icy planets.**

ammonia hydrate | pressure | phase transition | density functional theory

A remarkable number of recently and currently discovered exoplanets can be classified as super-Earths or mini-Neptunes, with masses up to 10 Earth masses and mean densities around 1 g/cm<sup>3</sup> (1–3). The uncertainty in classification hints at a substantial problem: Researchers cannot distinguish from afar whether these bodies are mostly rocky (like Earth) or mostly icy (like Neptune). Inside our own solar system, we have the “ice giants” Uranus and Neptune. We know their mantle region contains large amounts of water, ammonia, and methane ices, as well as hydrogen in various forms, while their cores are presumably formed by a small amount of heavy elements (4–7). However, even for those planets, observational data are limited to global observables such as mass, radius, and gravitational and magnetic moments. These provide only a loose set of constraints on interior composition, which can be satisfied by a variety of planetary models. The low luminosity of Uranus, for instance, could be due to a thermal boundary layer, which would suggest significant composition gradients inside its mantle (7–9). To constrain plausible interior models, more astrophysical data are needed (1). At the same time, laboratory experiments and accurate calculations are necessary to establish the equations of state of the planets’ potential constituent materials. As these constituents experience extreme pressure and temperature conditions inside the planets, many of their defining properties such as viscosity and thermal or electrical conductivity are likely to change drastically from what we are used to at ambient conditions. This is a consequence of qualitative differences that can emerge in chemical bonding, and even the stabilization of entirely new compounds and stoichiometries under compression (10–14). High-pressure studies of the individual molecular ices are therefore abundant,

both experimentally and theoretically. Systematic investigations of their mixtures are much more sparse, due to the increased complexity they introduce, although attempts at experimental and computational high-pressure studies on mixtures of molecular ices close to their solar abundance ratio have been performed (15, 16). However, it is not clear that this mixing ratio, roughly 4:1:7 of methane:ammonia:water (17, 18), plays a role inside any icy planets in their present state. Most pressingly, it is unknown how the different ices are distributed throughout the planetary interiors—Would they occur as homogeneous mixtures, exhibit continuous concentration gradients, or form stratified layers of specific compositions (6, 19, 20)?

All ices feature a ladder of interactions, ranging from covalent, ionic/electrostatic, and hydrogen bonding (not in methane) to weak dispersion interactions. It is the interplay of these interactions, and their relative emphasis as the molar volumes are reduced, that drive intriguing phase transitions, and the emergence of new structural features. Ammonia has been predicted to form an ionic crystal (NH<sub>4</sub>)<sup>+</sup>(NH<sub>2</sub>)<sup>-</sup> above 100 GPa (21), and this has recently been confirmed in experiment (22, 23). The energetic cost of breaking the N–H bond is outweighed by ionic bonding NH<sub>4</sub><sup>+</sup>⋯NH<sub>2</sub><sup>-</sup> and more compact packing. Water leaves the molecular state via another route, forming the atomic ice-X network structure with symmetric hydrogen bonds at 60 GPa (24), while, at terapascal pressures, it is predicted to take up more complex phases that can be seen as partially ionic OH<sup>-</sup>/H<sub>3</sub>O<sup>+</sup> (25, 26). At low temperatures, nuclear quantum effects are expected to influence the phase diagram of

## Significance

The mantles of icy planets comprise large amounts of water, ammonia, and methane ices. To understand their interior structure, it is crucial to study these ices at the extreme pressure conditions they likely experience. Hitherto, such studies have mostly been restricted to individual ices and not considered formation of stable mixtures. We survey here mixtures of water and ammonia and show that high pressures stabilize ammonia hemihydrate, through a transformation from a molecular crystal into a fully ionic solid that involves complete deprotonation of water. We suggest that ammonia-rich hydrates can precipitate out of any ammonia–water mixture at sufficient pressures and are an important component inside icy planets.

Author contributions: Y.M. and A.H. designed research; V.N.R. performed research; Y.W. contributed new reagents/analytic tools; V.N.R., Y.M., and A.H. analyzed data; and V.N.R., Y.W., Y.M., and A.H. wrote the paper.

The authors declare no conflict of interest.

This article is a PNAS Direct Submission.

Data deposition: Data reported in this paper have been deposited on The University of Edinburgh website, [datashare.is.ed.ac.uk/handle/10283/2777](https://datashare.is.ed.ac.uk/handle/10283/2777).

<sup>1</sup>To whom correspondence should be addressed. Email: [a.hermann@ed.ac.uk](mailto:a.hermann@ed.ac.uk).

This article contains supporting information online at [www.pnas.org/lookup/suppl/doi:10.1073/pnas.1706244114/-DCSupplemental](http://www.pnas.org/lookup/suppl/doi:10.1073/pnas.1706244114/-DCSupplemental).

hydrogen-bonded systems (27), while, at high temperatures, superionicity is predicted to occur in both water and ammonia: The heavy O/N atoms form crystalline lattices, while protons are free to diffuse through the crystal (28–30).

Among planetary ice mixtures, ammonia–water compounds are arguably of the most chemical interest, because they can form fully connected  $\text{HOH}\cdots\text{NH}_3$  and  $\text{H}_2\text{NH}\cdots\text{OH}_2$  hydrogen-bonded networks. Three stoichiometric mixtures exist in nature and close to ambient conditions: ammonia monohydrate (AMH,  $\text{NH}_3:\text{H}_2\text{O} = 1:1$ ), ammonia dihydrate (ADH, 1:2), and ammonia hemihydrate (AHH, 2:1) (31). Their phase diagrams are relatively complex: Six AMH phases, four ADH phases, and two AHH phases are known at various pressure–temperature (P–T) conditions, even though some of their structures have not been resolved. AHH has arguably been studied the least among the ammonia hydrates, possibly because of its high ammonia content, far removed from the solar abundance ratio 1:7, and is therefore expected to be rare in nature. However, it is a crucial phase at high pressure and temperature, where both ADH and AMH decompose into  $\text{AHH} + \text{ice-VII}$ , around 3 GPa and at 280 K and 250 K, respectively (32, 33). At slightly higher pressures (around 5 GPa to 20 GPa) and room temperature, all ammonia hydrates are found to form disordered molecular alloy (DMA) phases, which feature substitutional disorder of ammonia and water (maybe partially ionized into  $\text{OH}^-/\text{NH}_4^+$ ) on a body-centered cubic (bcc) lattice (33–36). The AHH DMA phase has been observed in two independent experiments (35, 36) that found, at low temperatures, transitions from AHH phase II at 19 GPa to 30 GPa. AHH DMA was found to remain stable up to the highest pressure studied, 41 GPa (36).

Previous first-principles calculations have been carried out to resolve high-pressure molecular phases in the ammonia hydrates (37, 38). In AMH, calculations predicted that an ionic phase transition should stabilize  $\text{NH}_4^+\cdot\text{OH}^-$  over  $\text{NH}_3\cdot\text{H}_2\text{O}$  around 6 GPa (39). A more stable ionic structure was proposed recently (40), and subsequent crystal structure searches on AMH uncovered higher-pressure ionic phases, which were then used as starting points for ab initio molecular dynamics (MD) simulations to investigate the superionic regime of AMH (41). These studies attempted to explore molecular mixtures at conditions present deep within icy planetary bodies using electronic structure calculations, but there is an inherent assumption that AMH is indeed a relevant stoichiometry at elevated pressures in the water–ammonia phase diagram. This assumption needs to be clarified by studies on other mixtures, first and foremost ADH and AHH, to ultimately construct a coherent picture of the inner structure of icy planets as dependent on overall composition.

Here, we present results from crystal structure predictions in conjunction with electronic structure calculations of compressed AHH. Above 65 GPa, beyond the stability regime of the DMA phase, we find a sequence of new high-pressure phases that ensure AHH remains a stable (and indeed dominant) composition within the water–ammonia phase diagram to very high pressures. The structures uncovered here are fully ionic and combine atomic  $\text{O}^{2-}$  anions and molecular  $\text{NH}_4^+$  cations. Oxides are a major thermodynamic sink and are found in virtually all fields of chemistry and materials science, but these ammonium oxide structures represent an example where water in a hydrate compound becomes completely deprotonated by application of pressure. A sequence of such structures remains stable up to 550 GPa and elevated temperatures, where decomposition into the constituents water and ammonia is predicted to occur.

## Results

Two structures of AHH have been solved, phases I and II. In experiments at  $T = 200$  K, the transition I→II is estimated to

occur around 1 GPa (36). In our ground-state calculations, this transition occurs at 4 GPa, slightly above the experimental estimate, but in line with the negative Clapeyron slope seen in experiment. In Fig. 1, we show the evolution of the relative ground-state enthalpies,  $\Delta H_f = H_f(\text{AHH}) - [H_f(\text{H}_2\text{O}) + 2H_f(\text{NH}_3)]$ , as a function of pressure on two different scales (0 GPa to 100 GPa and 50 GPa to 800 GPa), for the known and new phases. This represents the different phases' enthalpic stability toward decomposition into the molecular constituents of  $\text{H}_2\text{O}$  and  $\text{NH}_3$ , where, at each pressure, we have chosen the most stable  $\text{H}_2\text{O}$  and  $\text{NH}_3$  phases.

We also show, in Fig. 1, the relative enthalpies of potential decomposition products of AHH, namely  $H_f(\text{AMH} + \text{NH}_3)$  and  $1/2H_f(\text{ADH} + 3\text{NH}_3)$ . A decomposition of AHH into ADH and ammonia is never favorable; in fact, just below 100 GPa, we find ADH itself becomes unstable toward decomposition into water and ammonia ice. For AMH, we find that, at low pressures, a proposed tetragonal ionic  $\text{NH}_4^+\cdot\text{OH}^-$  phase (40) is, up to 28 GPa, more stable than AHH. This phase has not yet been seen in experiments on compressed AMH.

Among AHH phases, above 23 GPa in our calculations, AHH-II is followed by several quasi-bcc phases, which are indicated by the shaded region in Fig. 1 and which are energetically competitive up to 65 GPa. As a phase transition to a substitutionally disordered bcc structure has been observed at 19 GPa in room-temperature experiments, we would expect to find many competing quasi-bcc structures in this pressure region. All relevant structures we find in this region are half-ionized, i.e., of the composition  $\text{NH}_3\cdot\text{NH}_4^+\cdot\text{OH}^-$ , and feature hydrogen bonds. These structures are not immediately obvious to be quasi-bcc—see *SI Appendix* for full structural details—but occupy a pressure range where experiment has observed the bcc DMA structure. Upon closer inspection, the underlying quasi-bcc structure becomes apparent, both in real and reciprocal space: Representative structures feature locally quasi-cubic molecular arrangements, and their simulated powder X-ray diffraction peaks cluster around the peaks of an ideal bcc lattice (see *SI Appendix, Fig. S1*). This suggests that the structure search algorithms attempt to construct disordered phases in the pressure range around 20 GPa to 60 GPa. Similar results were also seen at low pressures, where AHH-I is stable: Searching the configuration space with too small unit cells to reproduce the actual phase I structure, which has 12 molecules in the unit cell, resulted in candidate structures that mimicked the molecular herringbone arrangements of AHH-I. In the gas phase with well-separated entities, the proton transfer process  $\text{NH}_3 + \text{H}_2\text{O} \rightarrow \text{NH}_4^+ + \text{OH}^-$  is endothermic by about 8 eV; it is enabled here by ionic bonding and a more compact packing of the constituents ( $\Delta V/V = -3.3\%$  for  $\text{AHH-II} \rightarrow A2/m$  at 20 GPa). It is possible that these structures

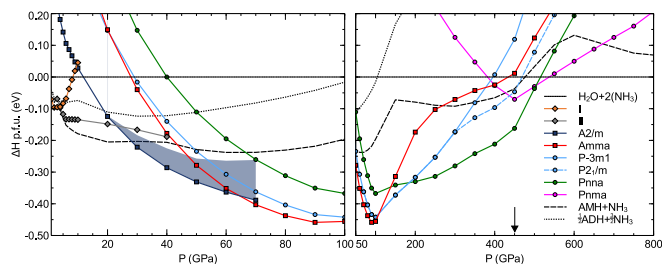


**Fig. 1.** Enthalpies of formation of AHH phases as a function of pressure, relative to decomposition into ice and ammonia (or  $2/5 \text{NH}_4 + 1/5 \text{N}_3\text{H}_7$  above 450 GPa; see arrow), shown in the range 0 GPa to 100 GPa (Left) and 50 GPa to 800 GPa (Right). The shaded region in Left denotes an approximate enthalpy range of quasi-bcc structures, with a lower bound by the most stable approximant we found (see *Results*). Dashed and dotted lines indicate decomposition reactions into other ammonia hydrates.

could be the basis of an ordered low-temperature form of the DMA phase for AHH. Experimentally, no further phase transitions have been observed in AHH up to 40 GPa.

At 63 GPa, we find in our calculations a new orthorhombic structure of *Amma* symmetry that is energetically most stable, with the intriguing attribute of doubly deprotonated water: all  $\text{H}_2\text{O}$  have donated both protons to two  $\text{NH}_3$  molecules, which results in a fully ionic ammonium oxide compound  $(\text{NH}_4^+)_2\text{O}^{2-}$ . At 110, 180, and 505 GPa in the ground state, we find three more phase transitions, first to a trigonal  $P\bar{3}m1$  structure, followed by two orthorhombic phases of *Pnna* and *Pnma* symmetry, and all with the same features of fully deprotonated water and molecular ammonium cations. These structures are shown in Fig. 2, and details of their crystal structures are tabulated in *SI Appendix*. The emergence of this sequence of ionic structures is responsible for the extended stability of AHH against decomposition into ice and ammonia to much larger pressures; see Fig. 1. We also find that ADH and AMH would decompose into AHH and appropriate amounts of ice at pressures above 60 and 85 GPa, respectively. Eventually, at 540 GPa in the ground state, we find that AHH decomposes into ice and ammonia. For this decomposition, we took into account recent computational work that found  $\text{NH}_3$  decomposes into  $\text{N}_3\text{H}_7$  and  $\text{NH}_4$ , which we find above 450 GPa [see arrow in Fig. 1, *Right* (42)]. Note that water ice is not expected to decompose until multiterapascal pressures are reached (43, 44).

It has been suggested that the Perdew–Burke–Ernzerhof (PBE) functional overstabilizes charge transfer in the  $\text{NH}_3 + \text{H}_2\text{O} \rightarrow \text{NH}_4^+ + \text{OH}^-$  reaction (38). We therefore reoptimized all structures using the PBE + TS functional, which includes the Tkatchenko–Scheffler (TS) dispersion correction scheme (45), and found little quantitative difference in the relevant structural evolution: The transition from half-ionic to fully ionic phases (the onset of stability of the *Amma* phase) is found at 58 GPa, while decomposition of the *Pnma* phase into the individual ices is calculated to occur at 458 GPa.

To estimate the effects of finite temperature, we calculated free energies for all phases using the quasi-harmonic approxima-

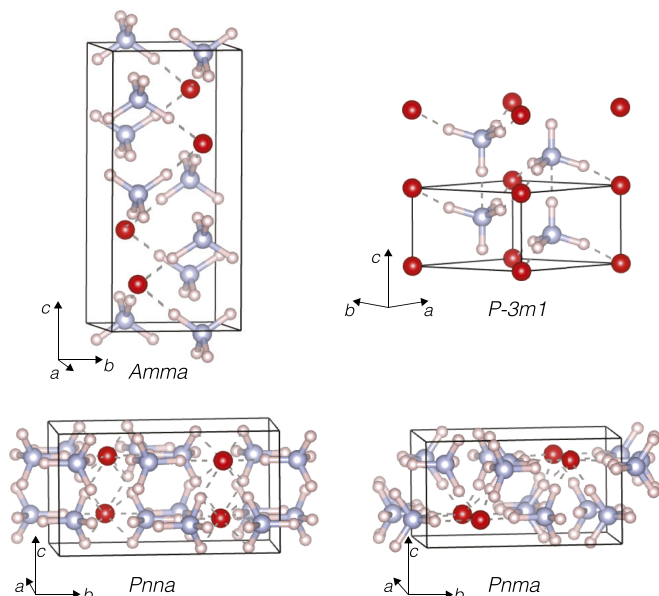


**Fig. 2.** Fully deprotonated AHH structures: *Amma* phase at 80 GPa (*Top Left*);  $P\bar{3}m1$  phase at 100 GPa (*Top Right*); *Pnna* phase at 300 GPa (*Bottom Left*); and *Pnma* phase at 600 GPa (*Bottom Right*). Red (blue, white) spheres denote O (N, H) atoms. All phases are drawn to the same scale, and hydrogen bonds from  $\text{NH}_4^+$  to O are shown as dashed lines.

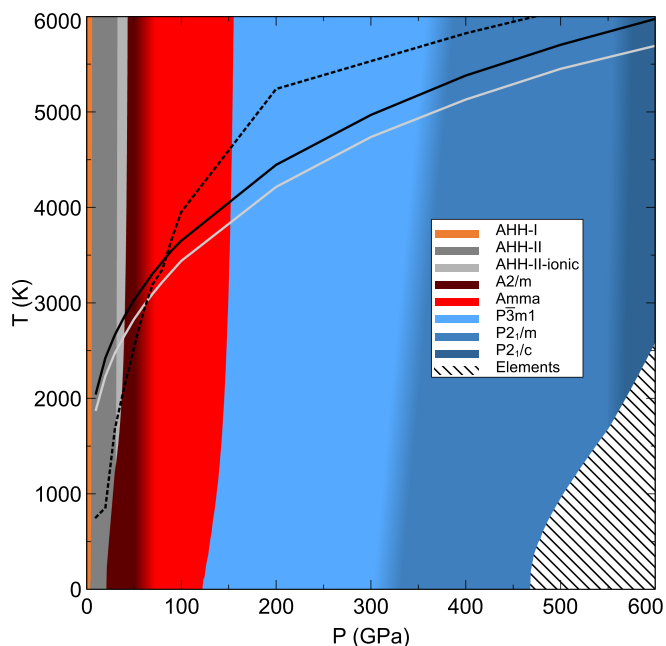


**Fig. 3.** P-T phase diagram of AHH phases, computed within the quasi-harmonic approximation. The dashed region at highest pressures represents predicted decomposition into the constituent ices. The dashed black line indicates the computed melting line of AMH (41), while solid black (gray) lines indicate calculated planetary isentropes of Uranus (Neptune) (46).

tion, which takes into account the vibrational entropy. The latter might well influence the phases' stability range, as we find quite a diverse chemistry in the progression from hydrogen-bonded molecular to fully ionic phases. Fig. 3 shows the resulting P-T phase diagram. This implies an earlier onset of stability for the fully ionic phases, with the *Amma* phase becoming stable at 40 GPa to 50 GPa at low temperatures, but also eventual decomposition at lower pressures than in the ground state, as low as 470 GPa, depending on temperature. The temperature dependence of the stability of most phases, apart from the eventual decomposition, is actually relatively weak, and changes compared with the ground-state results shown in Fig. 1 are mostly due to zero-point energy (ZPE) effects (see *SI Appendix*, Fig. S2 for a plot of  $H + \text{ZPE}$  as a function of pressure). This can be rationalized with the qualitative change in proton coordination at the ionization transition and its influence on the molecular vibron modes that will dominate the ZPE. We find that the stability region of the  $P\bar{3}m1$  phase is much increased, at the expense of the orthorhombic *Pnna* and *Pnma* phases. In fact, two monoclinic phases of  $P2_1/m$  and  $P2_1/c$  symmetry (see *SI Appendix*, Fig. S3), which are the results of soft phonon modes in  $P\bar{3}m1$  at very high pressures, become stable around 300 GPa to 350 GPa and 550 GPa, respectively, and dominate the high-pressure regime of the P-T phase diagram. For perspective, we show, in Fig. 3, the mantle isentropes of Uranus and Neptune, as well as the melting line of AMH obtained from MD simulations (41). Both melting and onset of superionicity (which we suspect occurs significantly below the melting line) are not considered in our quasi-harmonic approach here.

The deprotonation reaction of  $\text{OH}^-$  in the gas phase,  $\text{NH}_3 + \text{OH}^- \rightarrow \text{NH}_4^+ + \text{O}^{2-}$ , is endothermic by about 16 eV. This is twice the energy needed to remove the first proton off water, yet comes as a natural follow-up to the partial deprotonation of  $\text{H}_2\text{O}$ . The process requires (i) more compression work being exerted on the system and (ii) a proton acceptor molecule,  $\text{NH}_3$ . Highly compressed AHH provides both and, as a consequence, forms fully ionic compounds at high pressure. These are further

stabilized by more compact packing, facilitated by the presence of spherical  $O^{2-}$  anions. Some of the ionic phases resemble known structure types. The  $P\bar{3}m1$  structure, for instance, is (if we assume spherical  $NH_4^+$ ) the  $CdI_2$  structure type, a well-known  $AB_2$  ionic structure (47). The assignments of molecules in these high-pressure phases are supported by their structural properties: the longest nearest-neighbor N–H separations decrease from 1.10 Å in *Amma* at 60 GPa to 0.99 Å in *Pnma* at 600 GPa, while the shortest nearest-neighbor O···H separations decrease from 1.35 Å to 1.17 Å for the same structures and pressures. The O–H separations at 60 GPa, for instance, are well above the separations seen in molecular water in ice-VIII at the same pressure (1.03 Å). A topological Bader charge analysis (48) also supports the ionic picture suggested above. The partial charges on O/ $NH_4$  are  $-1.27/+0.64e$  at 100 GPa in *Amma*, and are almost constant across the entire pressure range:  $-1.28/+0.64e$  in  $P\bar{3}m1$  at 100 GPa,  $-1.30/+0.65e$  in *Pnma* at 300 GPa, and  $-1.26/+0.63e$  in *Pnma* at 600 GPa.

In Fig. 4, *Inset*, we show an electron localization function (ELF) isosurface and 2D cut for the  $P\bar{3}m1$  phase, which confirm the presence of covalent bonds along the N–H separations, and the lack thereof around the oxygen anion—For the latter, ELF reveals its closed-shell character, but there are no local ELF maxima between the  $O^{2-}$  and  $NH_4^+$  entities. Around the transition from the quasi-bcc phases, at 60 GPa, the *Amma* phase is more compact by 1.4% than the lowest-energy quasi-bcc phase. Further transitions lead to ever more compact arrangements:  $\Delta V/V = -0.7/-0.5\%$  at 120/300 GPa, the respective onsets of stability of the  $P\bar{3}m1$  and  $P2_1/m$  phases at room temperature. This is, in part, facilitated by higher coordination of the  $O^{2-}$  anion: Because of its spherical character, in absence of covalent bonds or localized lone pairs, it is a much more flexible hydro-

gen bond acceptor than  $H_2O$ , which prefers low-density tetrahedral coordination up to very high pressures (26). In *Amma* and  $P\bar{3}m1$ , the oxygen anion is sixfold coordinated to N–H bonds, which increases to eightfold coordination in *Pnma*.

The complete absence of O–H stretch modes in the ionic high-pressure AHH phases should aid their spectroscopic detection. In Fig. 4, we show the pressure evolution of the intramolecular N–H stretch modes up to 200 GPa, calculated within the harmonic approximation. Across phases I and II and the half-ionized quasi-bcc phases, the N–H vibron bands occupy a range that broadens from 3,300  $cm^{-1}$  to 3,500  $cm^{-1}$  at 1 atm to 3,000  $cm^{-1}$  to 3,500  $cm^{-1}$  at 40 GPa. These frequency ranges are in reasonable agreement with experimental data, but shifted by about 100  $cm^{-1}$ , likely due to anharmonic effects (35, 49). A significant change should be noticeable at the transition from quasi-bcc to completely ionized phases: There are no vibrational modes in the previously mentioned frequency range; instead, N–H stretch modes in the *Amma* phase occur at much higher frequencies, around 3,600  $cm^{-1}$  in our calculations, and increase strongly with pressure. These modes involve stretches along N–H··· $NH_4^+$  hydrogen bonds. Another set of modes increases very strongly from 2,700  $cm^{-1}$  at 40 GPa to 3,200  $cm^{-1}$  at 110 GPa, and involves stretches along N–H··· $O^{2-}$  hydrogen bonds. At the transition to  $P\bar{3}m1$  at 110 GPa, with a much simpler mode structure, both sets of vibrational frequencies decrease, by about 20  $cm^{-1}$  to 80  $cm^{-1}$ , but continue to rise significantly with further increased pressure. The continuous hardening of the molecular vibrons is an indication that the intramolecular bonds in the  $NH_4^+$  units strengthen under compression; neither phase shows signs of impending transitions to a network structure, for instance with symmetric N–H–O or N–H–N bonds.

Electronically, all high-pressure phases, due to charge and/or proton transfer, are wide-gap insulators. In *SI Appendix, Fig. S4*, we show the evolution of the electronic band gap as a function of pressure for the most relevant phases. At low pressures, up to about 100 GPa in some structures, the band gaps increase with pressure, an effect previously noted in molecular crystals with polar units, where compression creates competing effects of widening electronic bands and shifts of intramolecular orbital states (50, 51).

## Discussion

From our ground-state calculations, we deduce that compressed AHH goes through three distinct regimes as pressures are applied beyond the stability range of the known molecular phase II. First, above 10 GPa, a range of quasi-cubic, partially ionized structures are stabilized, by 100 meV per formula unit (f.u.) compared with phase II at 40 GPa; see Fig. 1. Subsequently, above 65 GPa, a sequence of fully ionic structures is stabilized, which feature the unusual motif of doubly deprotonated water (i.e.,  $O^{2-}$  anions). These structures benefit from ionic bonding and high coordination of hydrogen bonds. Finally, above 500 GPa, separation into the constituents ice and ammonia (which itself is likely to decompose into other hydronitrogens) becomes favorable. This general trend is unaffected by an increase in temperature, considered here within the quasi-harmonic approximation. However, ZPE effects lead to slightly different stability ranges for each phase, and promote distortions of the  $CdI_2$ -like  $P\bar{3}m1$  phase; the onset of fully ionic phases should occur around 40 GPa at room temperature. Close to ambient conditions, the formation of molecular ammonia–water compounds is aided by energetically favorable hydrogen bonds between the two species (52). With increased compression, a different factor contributes: Proton transfer, in particular in a 2:1-ammonia:water compound, results in large stabilization due to ionic interactions and higher packing densities.

Complete deprotonation of water molecules in a compound is an intriguing chemical motif, and we are not aware of its presence

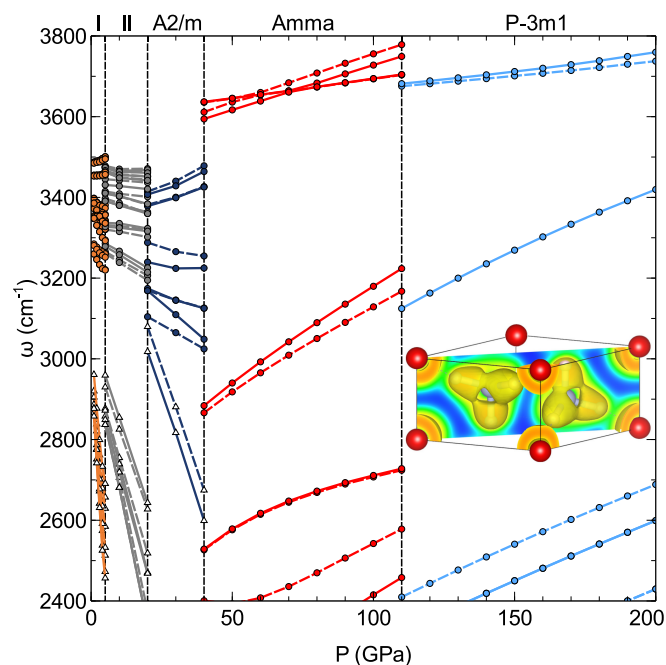


**Fig. 4.** Zone-centered vibrational frequencies of AHH phases in their respective room-temperature range of stability, focusing on the molecular vibron region of 2,400  $cm^{-1}$  to 3,800  $cm^{-1}$ . Phases are indicated along the top, and are colored as in Fig. 1. Solid (dashed) lines represent Raman (IR) active modes. Open triangles refer to OH stretch modes (seen until 40 GPa), and filled circles refer to NH stretches. (*Inset*) ELF plot for the  $P\bar{3}m1$  phase at 300 GPa. The isosurface value is 0.75, and 2D cut colors range from blue (ELF = 0) to red (ELF = 1).

in other hydrous systems. Water ionization can be achieved through thermal activation, for instance in ice or AMH, in transitions to superionic phases. In those temperature-induced transitions, protons are diffusive and free to move through a quasi-static lattice of the heavy nuclei. The triple points of solid, fluid, and superionic phases in water and AMH, estimated from simulations, are at  $(P, T) = (25 \text{ GPa}, 1,200 \text{ K})$  and  $(20 \text{ GPa}, 800 \text{ K})$ , respectively (28, 41). In AHH, the ionization of water is achieved through a different mechanism, purely through compression work, and the protons thus removed from the water molecules are not diffusive but bound in  $\text{NH}_4^+$  units instead. Higher pressures ( $P > 65 \text{ GPa}$ ) are needed to induce this ionization, but the resulting molecular units are arguably more strongly bound than in the lower-pressure region.

To investigate the high-pressure AHH phases more closely at the conditions expected in large icy planets, molecular dynamics calculations at elevated temperatures are required. One interesting question is whether a superionic region exists in AHH, and, if so, how the onset temperature of superionicity is affected by (i) the presence of heavy cation and anion species both and (ii) the seemingly increased N–H bond strengths in the molecular  $\text{NH}_4^+$  units as pressure increases. For ice, ammonia, and AMH, the onset temperatures of superionicity are calculated to be relatively insensitive to pressure (and therefore also insensitive to the underlying crystal structure) and to occur around 2,000, 1,000, and 1,000 K, respectively (28, 29, 41). In compressed AHH, the strongly bound ammonium cations could suggest that relatively high temperatures are needed to induce proton mobility, which, in turn, would lead to reduced thermal and electrical conductivity in any such layer present in planetary interiors.

Cosmic abundance ratios for ammonia:water are approximately 1:7, quite far removed from the 2:1 compound considered here. However, AHH is relevant at relatively low pressures, where it appears in the phase diagrams of both of the other known stoichiometric compounds: Both are more water-rich than AHH, but decompose into AHH-II and pure ice at appropriate P-T conditions. AHH is also very relevant at high pressures, and not just compared with the known AMH and ADH compositions: At 300 GPa, we find, in an extensive structure search across all  $(\text{NH}_3)_x(\text{H}_2\text{O})_{1-x}$  compounds (ranging from  $x = 1/6$  to  $x = 5/6$ ), that, besides the pure ices, only AHH is stable against decomposition; see the convex hull plot in *SI Appendix, Fig. S5*. It is therefore conceivable that AHH, driven by its ability to form completely ionic phases, precipitates out of any ammonia–water mixture under high-pressure conditions. At 300 GPa in our calculations, AHH- $P3m1$  has a density of

$3.50 \text{ g/cm}^3$ , which is 16% lighter than the most stable ice phase at the same pressure ( $Pbcm$  symmetry,  $4.17 \text{ g/cm}^3$ ). Thus, compressed water-rich ammonia–water mixtures in a planetary environment (e.g., in a 1:7 ratio or similar) could segregate into a layer of ammonia-rich ionic AHH solution above an ocean of pure water ice. The enthalpic gain achieved in this separation will need to compete with the entropy of mixing of the homogeneous mixture.

Another consequence of the prolonged stability of AHH under pressure is that ammonia reservoirs should always form compounds with water, at least until 450 GPa, where ammonia is predicted to decompose. Unless an icy planet's ammonia:water ratio is larger than 2:1, which is unlikely due to cosmic observations, ammonia will be unlikely to exist on its own up to pressures around 500 GPa, where we see demixing become favorable.

## Methods

Crystal structure prediction was performed using the particle swarm optimization algorithm as implemented in crystal structure analysis by particle swarm optimization (CALYPSO) code (53, 54) in conjunction with density functional total energy calculations. Structure predictions were performed with up to 4 f.u. of  $\text{H}_2\text{O}:\text{2}(\text{NH}_3)$ , i.e., 44 atoms, and at 5, 10, 20, 30, 50, 80, and 100 to 1,000 GPa in increments of 100 GPa. CALYPSO was able to recover a phase very close to the known AHH-II phase in the low-pressure searches. Searches above 800 GPa did not find any  $\text{H}_2\text{O}:\text{2}(\text{NH}_3)_2$  structures that were energetically favorable compared with decomposition into the constituent ices. The electronic structure calculations and geometry optimizations were performed with the CASTEP code (55). Exchange-correlation effects were described within the generalized gradient approximation (GGA) using the PBE functional (56), and adaptive ultrasoft pseudopotentials. Final structure relaxations were done with “hard” pseudopotentials with radii cutoffs no greater than 1.2 Å for oxygen and nitrogen, and 0.6 Å for hydrogen. Plane wave cutoffs of  $E_c = 1,000 \text{ eV}$  and k-point densities of 20 per angstrom were found to give sufficiently converged energies and forces.

Phonon calculations were performed for all structures using the finite displacement method as implemented in CASTEP (57), using supercells of at least 11 Å diameter in each direction. All structures presented here were found to be dynamically stable in their region of enthalpic stability, and dispersion curves are included in *SI Appendix*.

**ACKNOWLEDGMENTS.** We thank G. J. Ackland and J. S. Loveday for discussions. This research was supported by the UK's Engineering and Physical Sciences Research Council through the Condensed Matter Center for Doctoral Training (EP/L015110/1). Computational resources provided by the UK's National Supercomputer Service through the UK Car-Parrinello consortium (EP/K01465X), project d56 “Planetary Interiors,” and by the Royal Society (RG-150247) are gratefully acknowledged. Y.W. and Y.M. acknowledge funding support from National Natural Science Foundation of China under Grant 11534003 and National Key Research and Development Program of China under Grant 2016YFB0201200.

- Rauer H, et al. (2014) The PLATO 2.0 mission. *Exper Astron* 38:249–330.
- Sotin C, Grasset O, Mocquet A (2007) Mass–radius curve for extrasolar Earth-like planets and ocean planets. *Icarus* 191:337–351.
- Valencia D, Sasselov DD, O'Connell RJ (2007) Radius and structure models of the first super-Earth planet. *Astrophys J* 656:545–551.
- Hubbard WB, MacFarlane JJ (1980) Structure and evolution of Uranus and Neptune. *J Geophys Res Solid Earth* 85:225–234.
- Ross M (1981) The ice layer in Uranus and Neptune—Diamonds in the sky? *Nature* 292:435–436.
- Hubbard W, et al. (1991) Interior structure of Neptune: Comparison with Uranus. *Science* 253:648–651.
- Podolak M, Weizman A, Marley M (1995) Comparative models of Uranus and Neptune. *Planet Space Sci* 43:1517–1522.
- Hubbard WB, Podolak M, Stevenson DJ (1995) The interior of Neptune. *Neptune and Triton*, ed Cruikshank DP (Arizona Univ Press, Tucson, AZ), pp 109–138.
- Nettelmann N, et al. (2016) Uranus evolution models with simple thermal boundary layers. *Icarus* 275:107–116.
- Miao MS (2013) Caesium in high oxidation states and as a p-block element. *Nat Chem* 5:846–852.
- Zhang W, et al. (2013) Unexpected stable stoichiometries of sodium chlorides. *Science* 342:1502–1505.
- Zhu L, Liu H, Pickard CJ, Zou G, Ma Y (2014) Reactions of xenon with iron and nickel are predicted in the Earth's inner core. *Nat Chem* 6:644–648.
- Hermann A, Schwerdtfeger P (2014) Xenon suboxides stable under pressure. *J Phys Chem Lett* 5:4336–4342.
- Dewaele A, et al. (2016) Synthesis and stability of xenon oxides  $\text{Xe}_2\text{O}_5$  and  $\text{Xe}_3\text{O}_2$  under pressure. *Nat Chem* 8:784–790.
- Chau R, Hamel S, Nellis WJ (2011) Chemical processes in the deep interior of Uranus. *Nat Commun* 2:203.
- Meyer ER, et al. (2015) Bonding and structure in dense multi-component molecular mixtures. *J Chem Phys* 143:164513.
- Stevenson DJ (1992) Interior of Titan. *ESA Spec Publ* 338:29–33.
- Benvenuto OG, Fortier A, Brunini A (2009) Forming Jupiter, Saturn, Uranus and Neptune in few million years by core accretion. *Icarus* 204:752–755.
- Helled R, Anderson JD, Podolak M, Schubert G (2011) Interior models of Uranus and Neptune. *Astrophys J* 726:15.
- Nettelmann N, Helled R, Fortney JJ, Redmer R (2013) New indication for a dichotomy in the interior structure of Uranus and Neptune from the application of modified shape and rotation data. *Planet Space Sci* 77:143–151.
- Pickard CJ, Needs R (2008) Highly compressed ammonia forms an ionic crystal. *Nat Mater* 7:775–779.
- Palasyuk T, et al. (2014) Ammonia as a case study for the spontaneous ionization of a simple hydrogen-bonded compound. *Nat Commun* 5:3460.
- Ninet S, et al. (2014) Experimental and theoretical evidence for an ionic crystal of ammonia at high pressure. *Phys Rev B* 89:174103.
- Loubeyre P, LeToullec R, Wolanin E, Hanfland M, Hausermann D (1999) Modulated phases and proton centring in ice observed by X-ray diffraction up to 170 gpa. *Nature* 397:503–506.
- Wang Y, et al. (2011) High pressure partially ionic phase of water ice. *Nat Commun* 2:563.

26. Hermann A, Ashcroft NW, Hoffmann R (2012) High pressure ices. *Proc Natl Acad Sci USA* 109:745–750.
27. Ceriotti M, et al. (2016) Nuclear quantum effects in water and aqueous systems: Experiment, theory, and current challenges. *Chem Rev* 116:7529–7550.
28. Cavazzoni C, et al. (1999) Superionic and metallic states of water and ammonia at giant planet conditions. *Science* 283:44–46.
29. Bethkenhagen M, French M, Redmer R (2013) Equation of state and phase diagram of ammonia at high pressures from ab initio simulations. *J Chem Phys* 138:234504.
30. French M, Desjarlais MP, Redmer R (2016) Ab initio calculation of thermodynamic potentials and entropies for superionic water. *Phys Rev E* 93:022140.
31. Fortes AD, Choukroun M (2010) Phase behaviour of ices and hydrates. *Space Sci Rev* 153:185–218.
32. Loveday JS, Nelmes RJ (2004) The ammonia hydrates—Model mixed-hydrogen-bonded systems. *High Press Res* 24:45–55.
33. Fortes AD, et al. (2007) The high-pressure phase diagram of ammonia dihydrate. *High Press Res* 27:201–212.
34. Loveday J, Nelmes R (1999) Ammonia monohydrate VI: A hydrogen-bonded molecular alloy. *Phys Rev Lett* 83:4329–4332.
35. Ma C, et al. (2012) Ammonia molecule rotation of pressure-induced phase transition in ammonia hemihydrates  $2\text{NH}_3 \cdot \text{H}_2\text{O}$ . *RSC Adv* 2:4920–4924.
36. Wilson C, et al. (2015) On the stability of the disordered molecular alloy phase of ammonia hemihydrate. *J Chem Phys* 142:094707.
37. Fortes AD, Suard E, Lemée-Cailleau MH, Pickard CJ, Needs RJ (2009) Crystal structure of ammonia monohydrate phase II. *J Am Chem Soc* 131:13508–13515.
38. Griffiths GIG, Fortes AD, Pickard CJ, Needs RJ (2012) Crystal structure of ammonia dihydrate II. *J Chem Phys* 136:174512.
39. Fortes AD, Brodholt JP, Wood IG, Vočadlo L, Jenkins H (2001) Ab initio simulation of ammonia monohydrate ( $\text{NH}_3 \cdot \text{H}_2\text{O}$ ) and ammonium hydroxide ( $\text{NH}_4\text{OH}$ ). *J Chem Phys* 115:7006–7014.
40. Griffiths GI, Misquitta AJ, Fortes AD, Pickard CJ, Needs RJ (2012) High pressure ionic and molecular crystals of ammonia monohydrate within density functional theory. *J Chem Phys* 137:064506.
41. Bethkenhagen M, Cebulla D, Redmer R, Hamel S (2015) Superionic phases of the 1:1 water–ammonia mixture. *J Phys Chem A* 119:10582–10588.
42. Qian GR, Hu CH, Oganov AR, Zeng Q, Zhou HY (2016) Diverse chemistry of stable hydronitrogens, and implications for planetary and materials sciences. *Sci Rep* 6:25947.
43. Zhang S, Wilson HF, Driver KP, Militzer B (2013)  $\text{H}_2\text{O}$  and other hydrogen-oxygen compounds at giant-planet core pressures. *Phys Rev B* 87:024112.
44. Pickard CJ, Martinez-Canales M, Needs RJ (2013) Decomposition and terapascal phases of water ice. *Phys Rev Lett* 110:245701.
45. Tkatchenko A, Scheffler M (2009) Accurate molecular van der Waals interactions from ground-state electron density and free-atom reference data. *Phys Rev Lett* 102:073005.
46. Redmer R, Mattsson TR, Nettelmann N, French M (2011) The phase diagram of water and the magnetic fields of Uranus and Neptune. *Icarus* 211:798–803.
47. Galasso FS, Kurti N, Smoluchowski R (1970) *Structure and Properties of Inorganic Solids* (Pergamon, Oxford).
48. Bader RFW (1994) *Atoms in Molecules: A Quantum Theory* (Oxford Univ Press, Oxford).
49. Mitev PD, Gajewski G, Hermansson K (2009) Anharmonic OH vibrations in brucite: Small pressure-induced redshift in the range 0–22 GPa. *Am Mineral* 94:1687–1697.
50. Hermann A, Schmidt WG, Schwerdtfeger P (2008) Resolving the optical spectrum of water: Coordination and electrostatic effects. *Phys Rev Lett* 100:207403.
51. Hermann A, Schwerdtfeger P (2011) Blueshifting the onset of optical UV absorption for water under pressure. *Phys Rev Lett* 106:187403.
52. Dill JD, Allen LC, Topp WC, Pople JA (1975) A systematic study of the nine hydrogen-bonded  $\text{OH}_2$ , and HF dimers involving  $\text{NH}_3$ ,  $\text{OH}_2$ , and HF. *J Am Chem Soc* 97:7220–7226.
53. Wang Y, Lv J, Zhu L, Ma Y (2010) Crystal structure prediction via particle-swarm optimization. *Phys Rev B* 82:094116.
54. Wang Y, Lv J, Zhu L, Ma Y (2012) CALYPSO: A method for crystal structure prediction. *Computer Phys Commun* 183:2063–2070.
55. Segall M, et al. (2002) First-principles simulation: Ideas, illustrations and the CASTEP code. *J Phys Condens Matter* 14:2717–2744.
56. Hammer B, Hansen LB, Nørskov JK (1999) Improved adsorption energetics within density-functional theory using revised Perdew-Burke-Ernzerhof functionals. *Phys Rev B* 59:7413–7421.
57. Ackland G, Warren M, Clark S (1997) Practical methods in ab initio lattice dynamics. *J Phys Condens Matter* 9:7861–7872.

# Stabilization of ammonia-rich hydrate inside icy planets

## Supplementary Information

Victor Naden Robinson<sup>a</sup>, Yanchao Wang<sup>b</sup>, Yanming Ma<sup>b,c</sup>, and Andreas Hermann<sup>a,1</sup>

<sup>a</sup>Centre for Science at Extreme Conditions and SUPA, School of Physics and Astronomy, The University of Edinburgh, Edinburgh, EH9 3FD, United Kingdom

<sup>b</sup>State Key Laboratory of Superhard Materials, College of Physics, Jilin University, Changchun 130012, China

<sup>c</sup>International Center for Future Science, Jilin University, Changchun 130012, China

<sup>1</sup>a.hermann@ed.ac.uk

### ABSTRACT

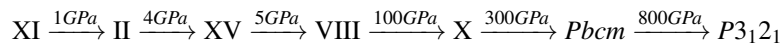
This supplementary material for "Stabilization of ammonia-rich hydrate inside icy planets" includes

- Pure ices' phase sequence
- Quasi-bcc AHH phases
- Zero-point energies
- High-pressure monoclinic crystal structures
- Electronic band gap, pressure evolution
- Structure search results across entire H<sub>2</sub>O-NH<sub>3</sub> binary phase space
- Oxygen atom H-coordination
- Phonon dispersions
- Crystallographic information.

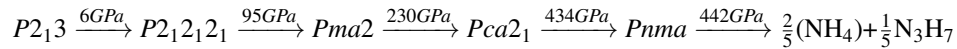
## Water Ammonia Phase Sequence

The phase sequence used for the baseline of  $\text{H}_2\text{O}+2(\text{NH}_3)$  is

$\text{H}_2\text{O}$



$\text{NH}_3$



Note that for ammonia the low pressure  $\text{Pa}\bar{3}$  phase was not included, and instead the experimental  $\text{P2}_1\text{3}$  phase was used.

These two phases differ in enthalpy by up to 7 meV per ammonia unit.

Above 442 GPa,  $\text{NH}_3$  decomposes as  $\text{NH}_3 \rightarrow \frac{2}{5}(\text{NH}_4)+\frac{1}{5}\text{N}_3\text{H}_7$ . At 450 GPa,  $\text{NH}_4$  takes a phase with space group  $C2/c$ , and  $\text{N}_3\text{H}_7$  has space group  $\text{P2}_1/m$ .



## Quasi-body centered cubic phases

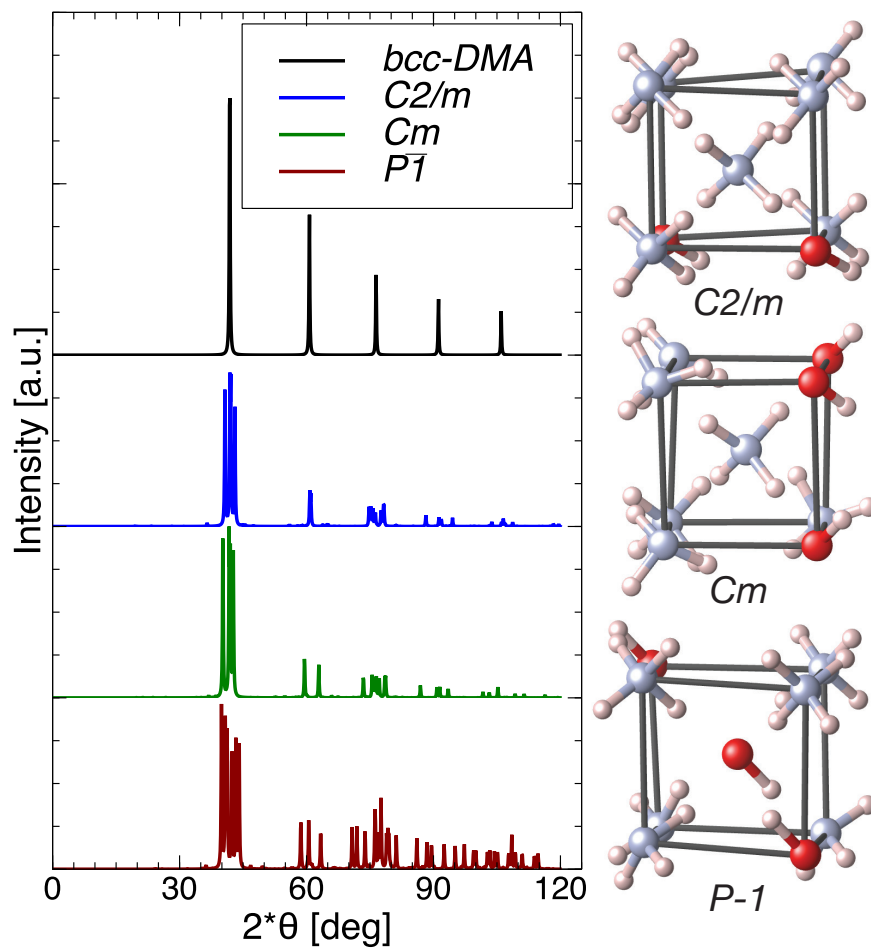


**Figure S1.** XRD patterns of representative quasi-BCC phases found in our structure searches, all simulated at 40 GPa, and labelled by space group. Right hand side shows some of the near-cubic local arrangements of each structure (black lines are guide to the eye and not unit cells). Red (blue, white) spheres denote O (N, H) atoms. The "bcc-DMA" pattern is for an idealised disordered bcc lattice with 2:1 N:O site occupancy and  $a=3.05\text{\AA}$ .

## Zero-point energies

We show in Figure S2 the enthalpies  $H = U + PV$  plus contributions from vibrational zero point energies (ZPE). Note at high pressures the extended stability region of the  $P\bar{3}m1$  phase and its symmetry-reduced variant  $P2_1/m$ , while the orthorhombic phases  $Pnna$  and  $Pnma$  are less relevant than in the ground state (see main manuscript).

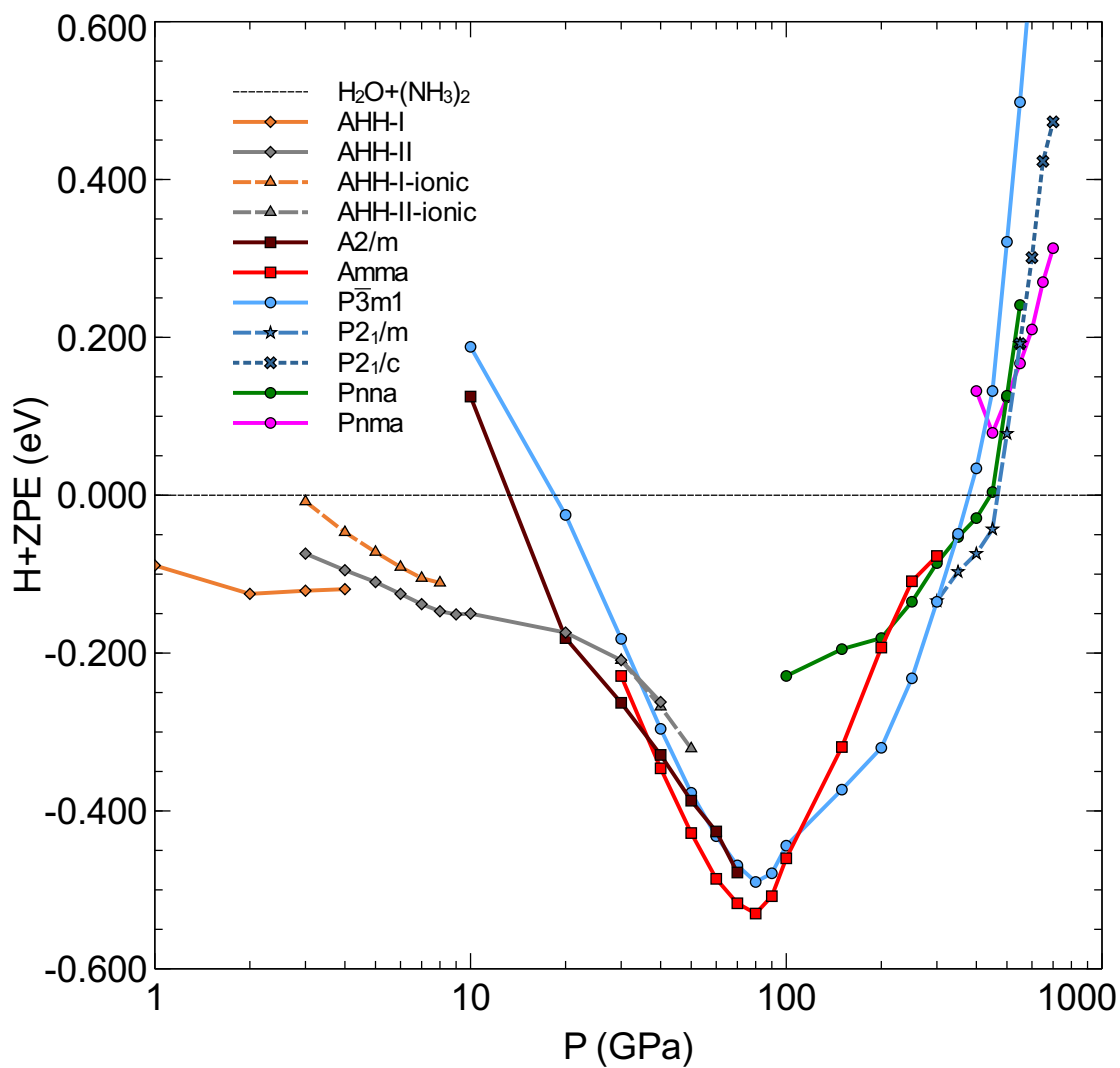


**Figure S2.** Phase diagram for ammonia hemihydrate based on  $H + ZPE$  calculations, and plotted on a logarithmic pressure scale.

## High-pressure monoclinic crystal structures

The monoclinic phases  $P2_1/m$  and  $P2_1/c$ , which feature in Figures 1 and 3 in the main manuscript, were obtained by following imaginary phonon modes that develop successively in the  $P\bar{3}m1$  crystal structure at high pressure.  $P2_1/m$  is monoclinic distortion of the highly symmetric  $P\bar{3}m1$  structure, whereas  $P2_1/c$  is a symmetry-broken variant of the  $P2_1/m$  structure. Both are shown in Figure S3 below.

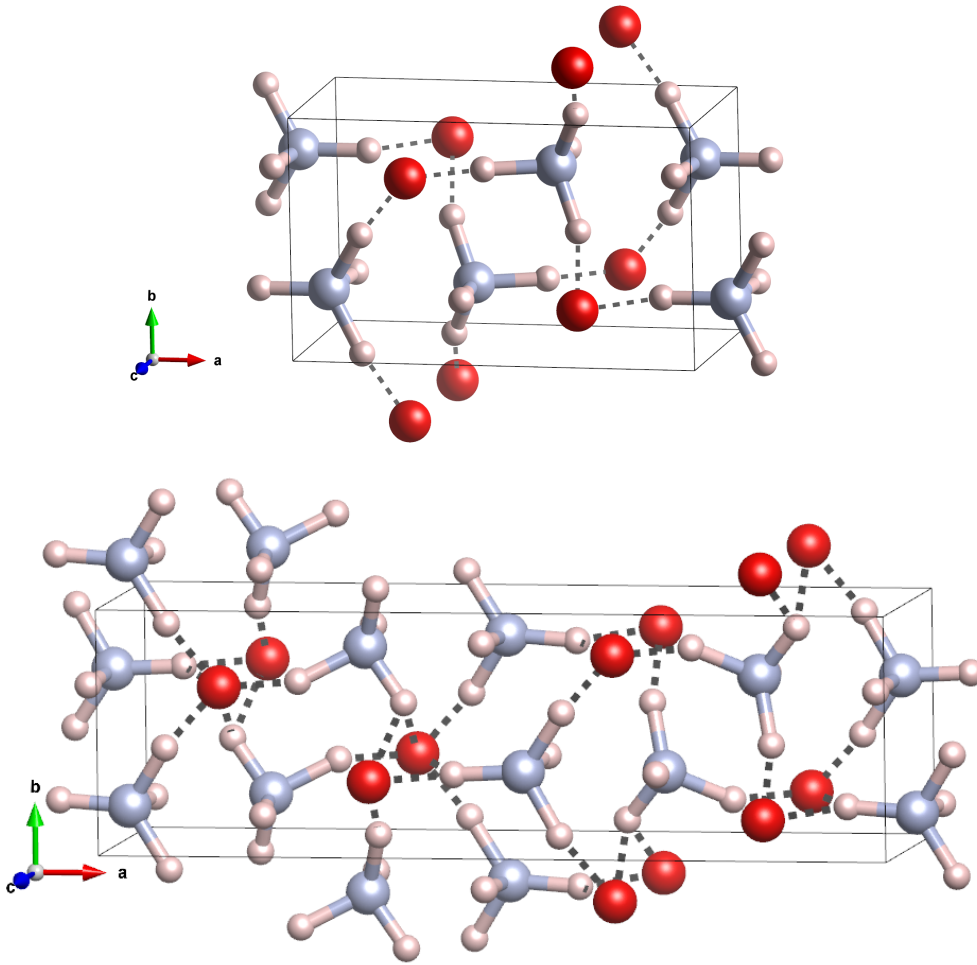


**Figure S3.** Top: monoclinic phase  $P2_1/m$  at 400 GPa; bottom: monoclinic phase  $P2_1/c$  at 650 GPa.

## Electronic band gap

We show in Figure S4 the evolution of the electronic band gap in AHH as function of pressure, across the various phase transition into eventual decomposition. Note that the single-particle DFT gaps are very likely to underestimate the actual electronic band gaps in all phases.

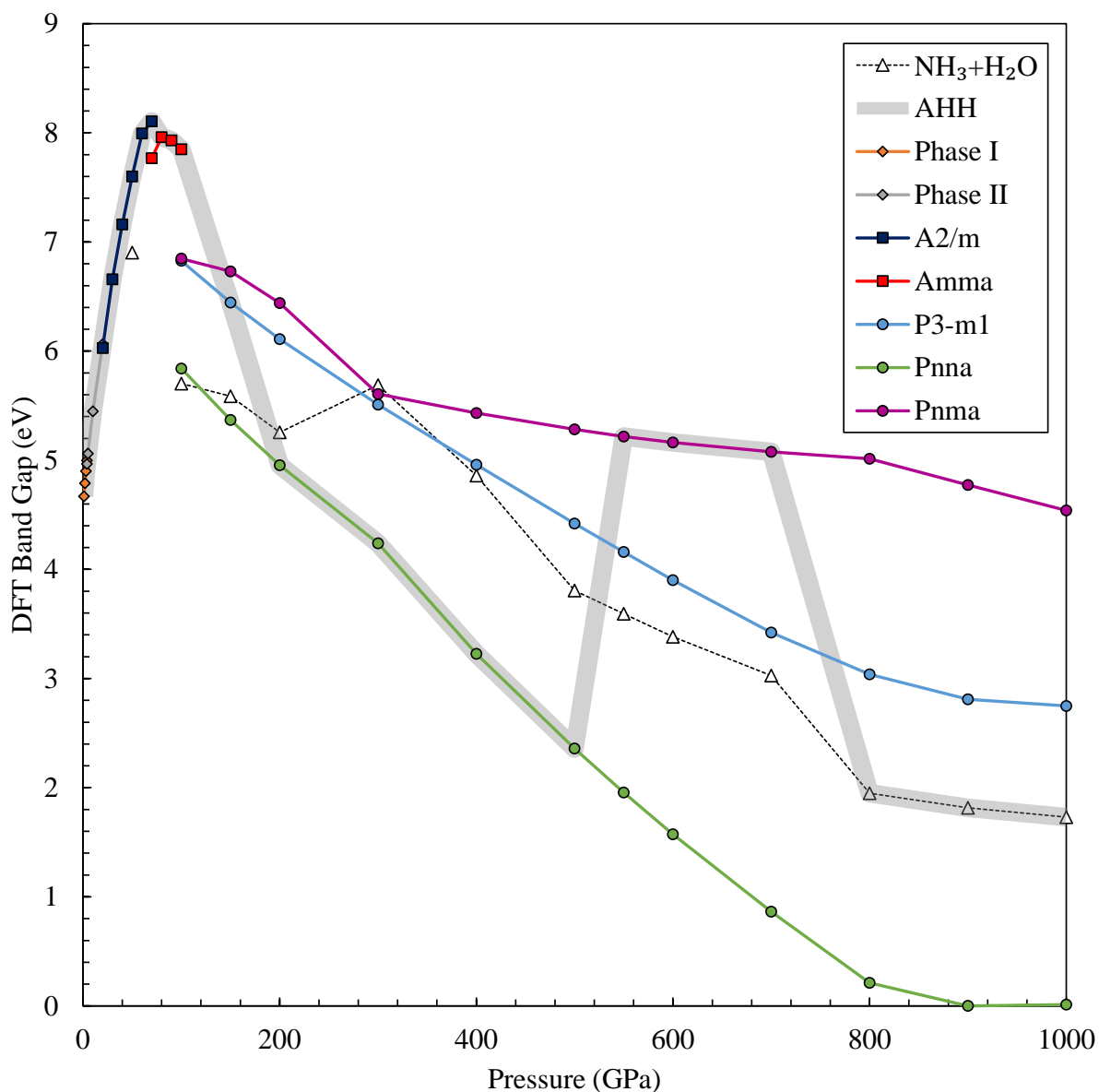


**Figure S4.** Electronic band gaps for various phases at different pressures, as obtained from DFT-PBE calculations. Shaded line follows the respective most stable AHH phase at every pressure.

## Convex hull at P=300GPa

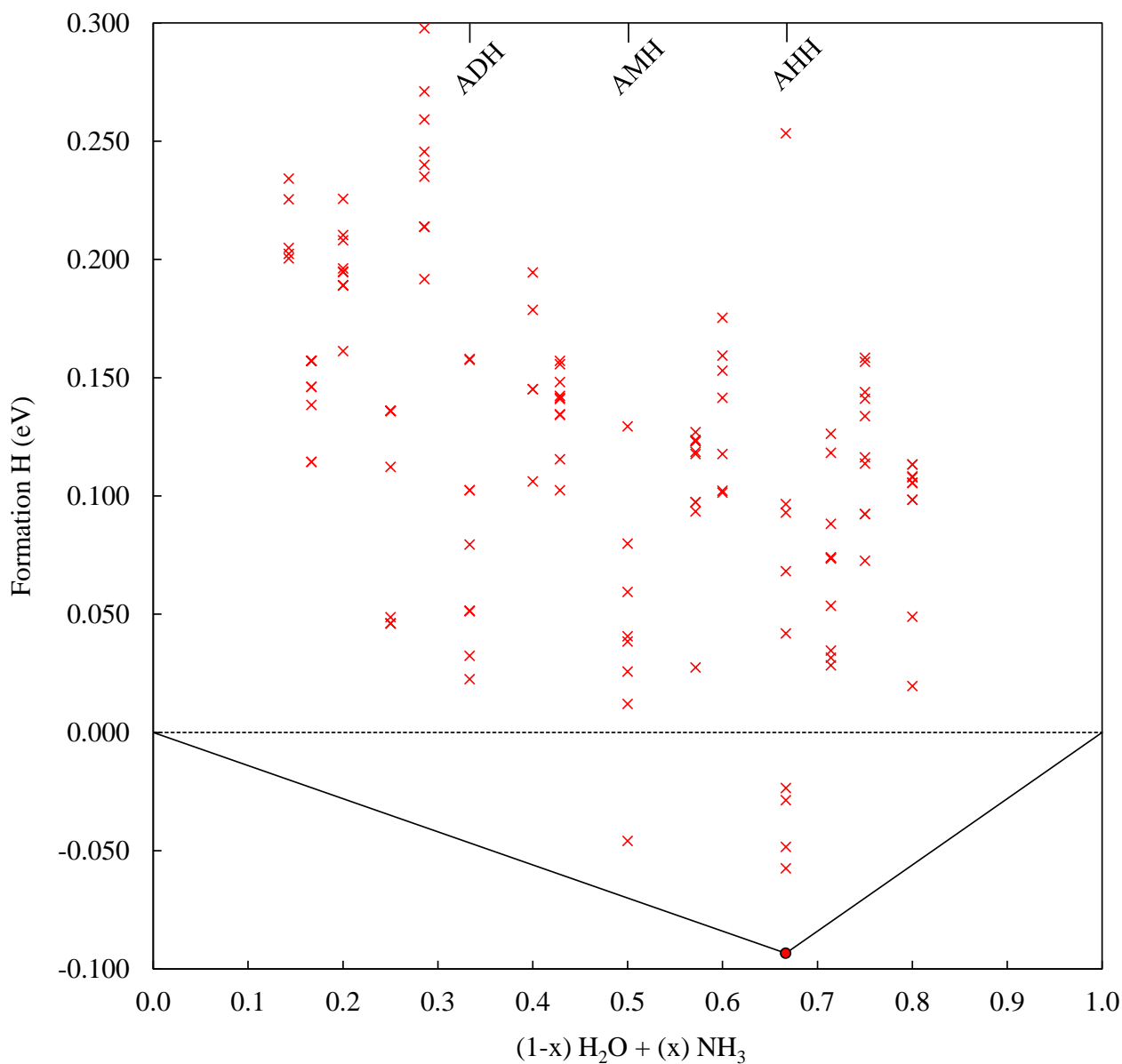


**Figure S5.** Convex hull data for mixing ratios from 6:1 to 1:5 for the binary ( $\text{H}_2\text{O}:\text{NH}_3$ ) system. The lowest enthalpy structures from structure searching with CALYPSO are plotted. Up to 4000 structures were optimized at a given mixing ratio. The ice phases forming the convex hull are taken to be  $Pbca$  for  $\text{H}_2\text{O}$  and  $Pca2_1$  for  $\text{NH}_3$ .

## Oxygen coordination

We show in Figure S6 the evolution of the average H-coordination of the oxygen atoms in AHH as function of pressure. Above 65 GPa, there are no more donated hydrogen bonds, as all water/hydroxyl molecules are completely deprotonated.

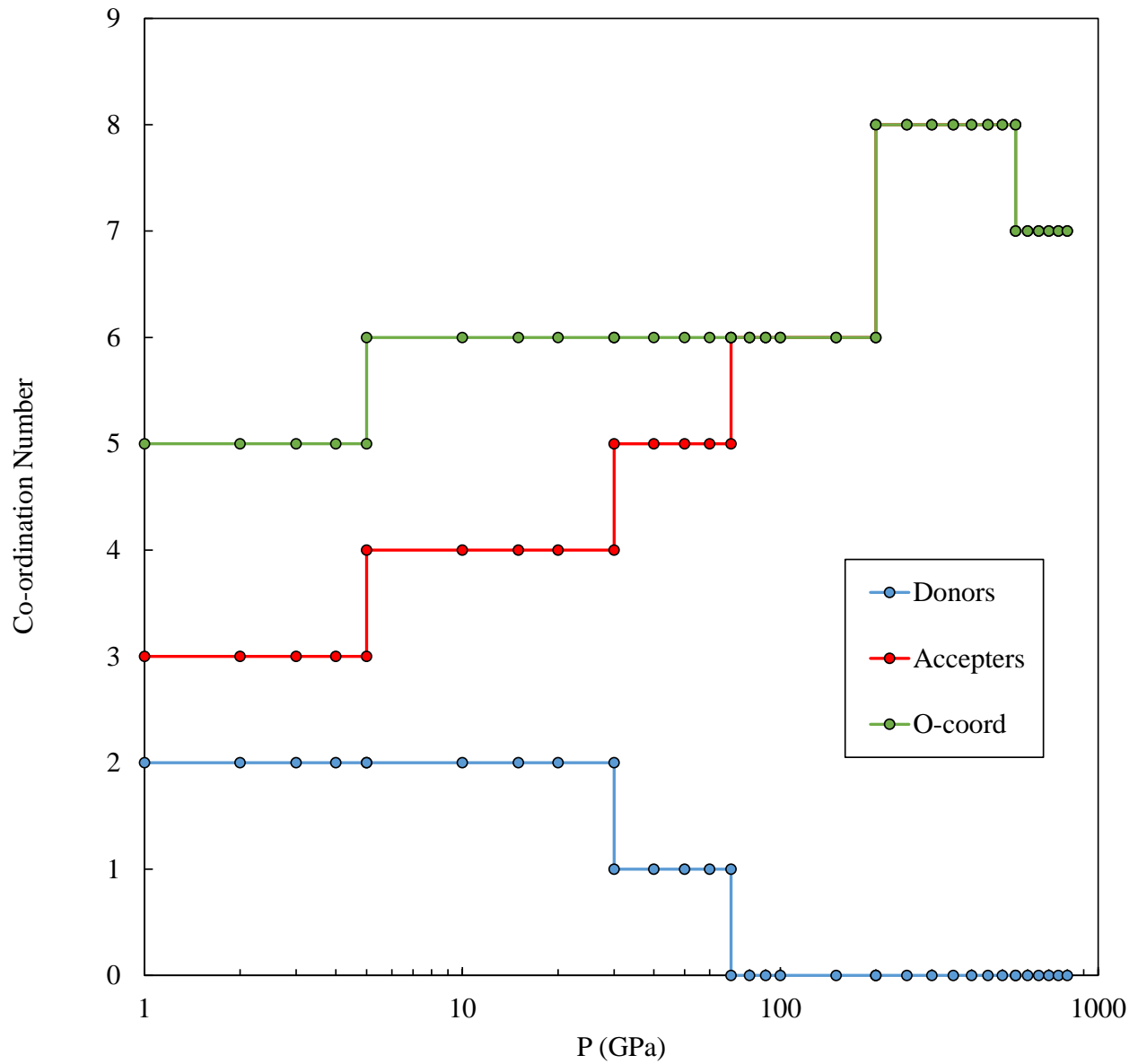


**Figure S6.** Oxygen coordination number in terms of hydrogen bonds.

## Phonon dispersions

Below, we show the phonon dispersion relations for all phases discussed in the main manuscript at pressure points relevant to their respective stability range. For the monoclinic phases points have the following coordinates:

$$\begin{aligned}
 Z &= (0,0,1/2) & \Gamma &= (0,0,0) & Y &= (0,1/2,0) & A &= (-1/2,1/2,0) \\
 B &= (-1/2,0,0) & D &= (-1/2,0,1/2) & E &= (-1/2,1/2,1/2) & C &= (0,1/2,1/2)
 \end{aligned}$$

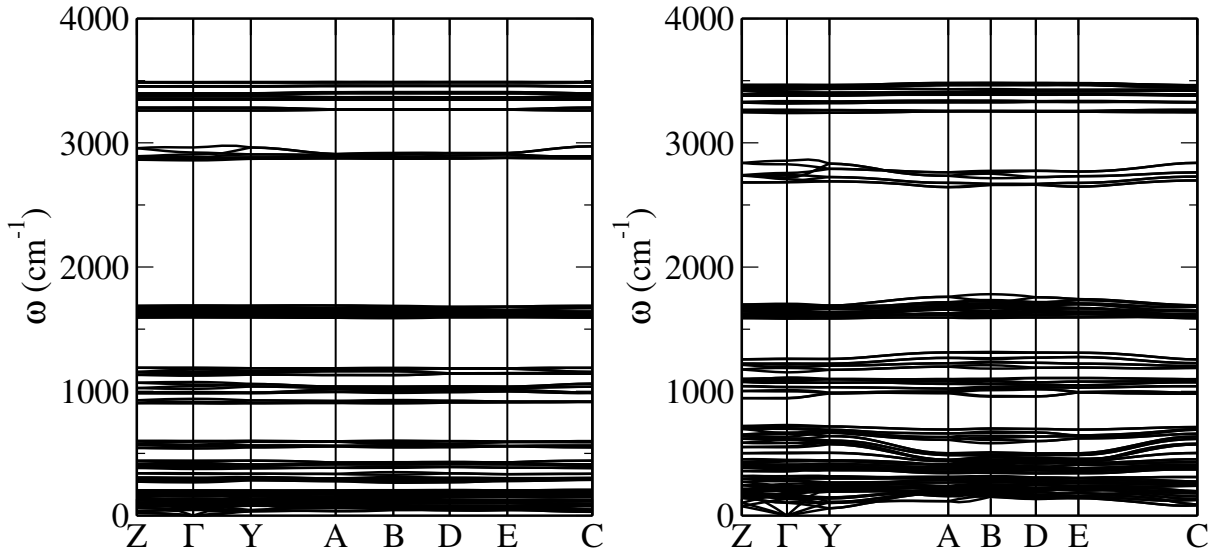


**Figure S7.** Left: AHH-I at 1 GPa; right: AHH-II at 10 GPa.

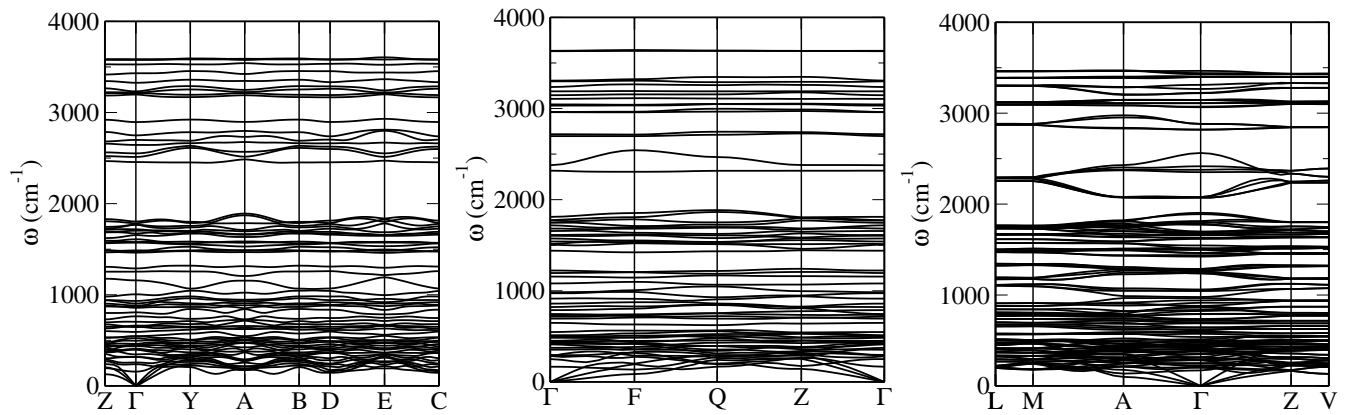


**Figure S8.** From left:  $Cm$ ,  $P\bar{1}$ , and  $A2/m$  phases, all at 30 GPa.

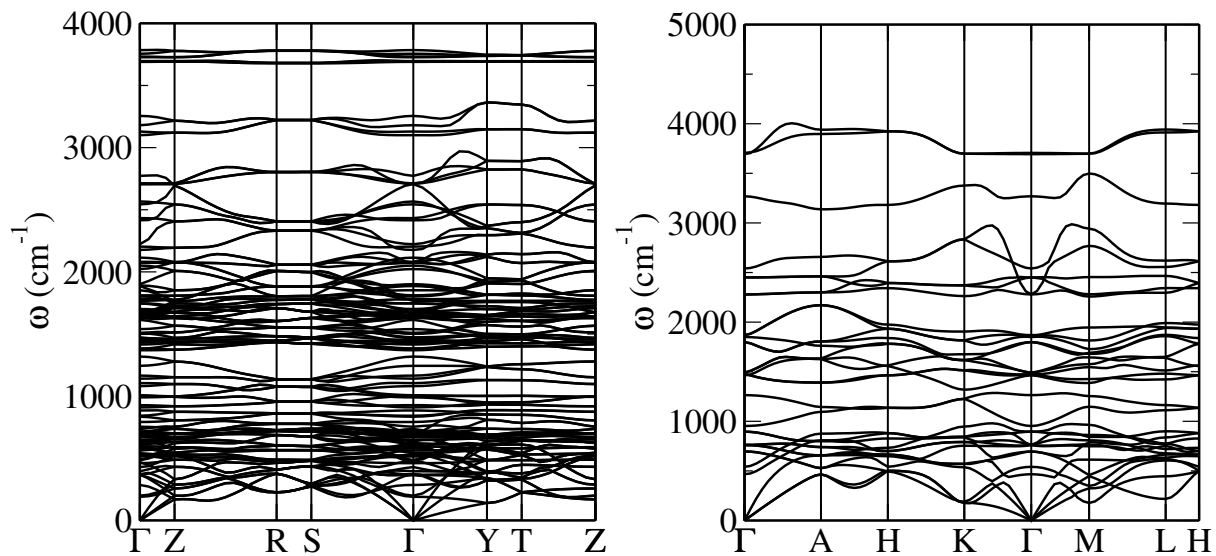


**Figure S9.** Left:  $Amma$  at 100 GPa; right:  $P\bar{3}m1$  at 150 GPa.

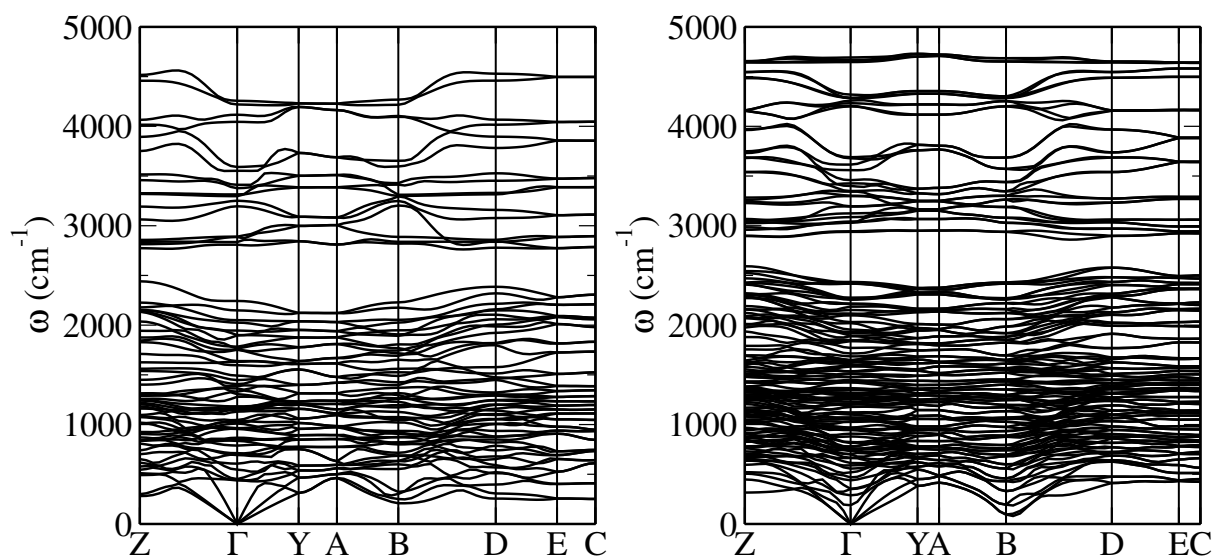


**Figure S10.** Left:  $P2_1/m$  at 400 GPa; right:  $P2_1/c$  at 650 GPa.



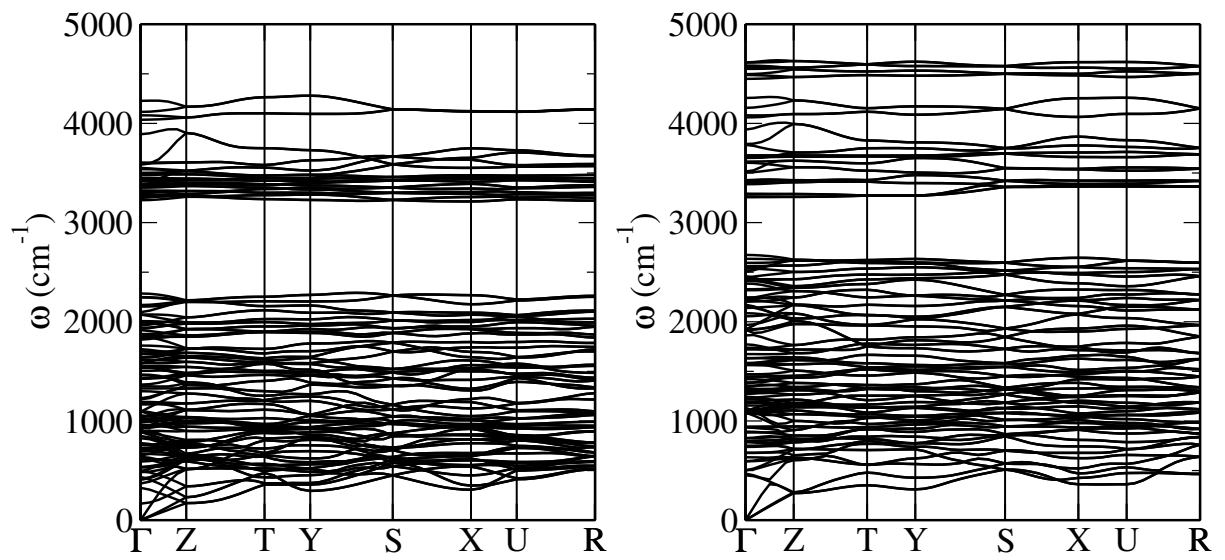


**Figure S11.** Left: *Pnna* at 300 GPa; right: *Pnma* at 700 GPa.

## Phase I and II data

AHH-I is proton-disordered on one ammonia site. We used an ordered approximate of the unit cell with space group  $P2_1/c$  in our calculations. Within the AHH-I unit cell, there are five distinct structures to choose the proton ordering. As Figure S12 shows, the relative enthalpy difference between these five structures is very small.

AHH-II is proton-ordered with space group  $P2_1/c$ .

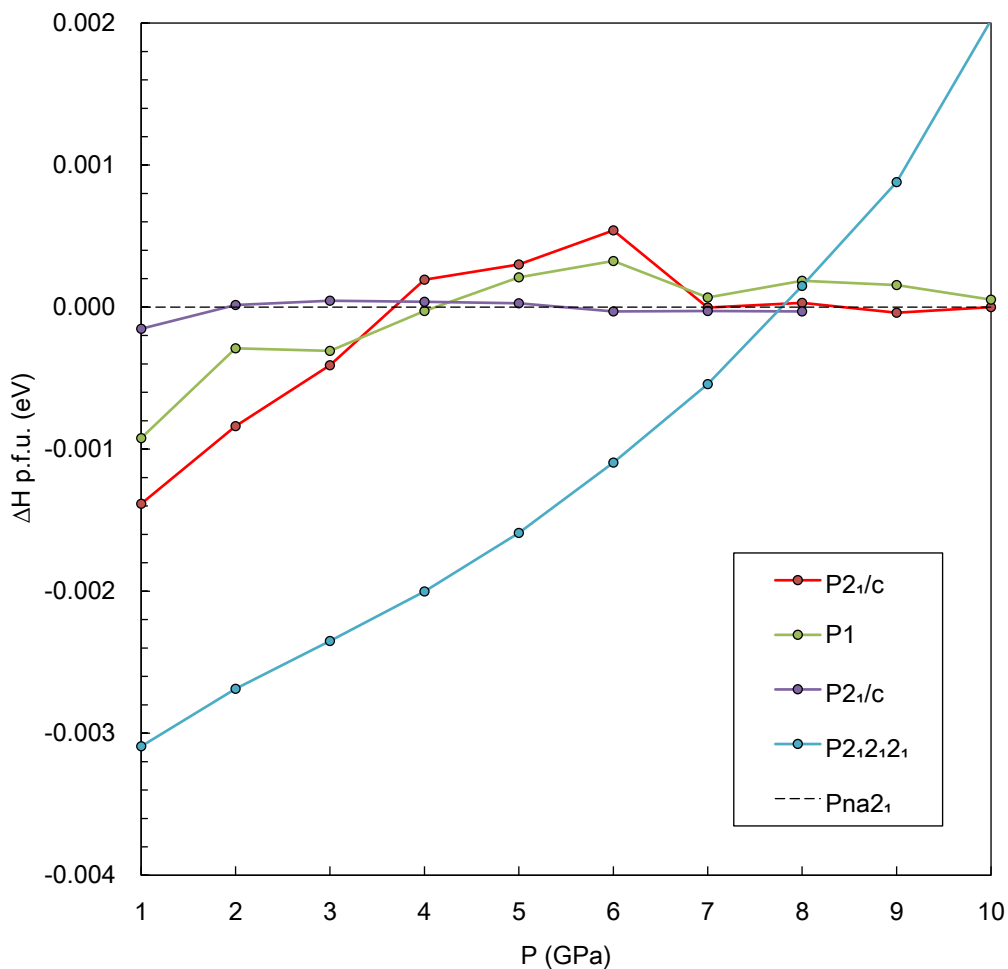


**Figure S12.** Calculated enthalpies for 5 unique variations of AHH-I.

## Crystallographic information

In the following tables, we give the crystal structures of the AHH phases discussed in the main manuscript, each at a relevant pressure point.

<i>A2/m</i> at 40 GPa			
Lattice Parameters	(Å)	(°)	
	a=5.01170	$\alpha=90.35538$	
	b=5.01170	$\beta=90.35538$	
	c=4.42760	$\gamma=49.49192$	
Atom	x	y	z
H1	-1.401262	0.001637	1.261673
H2	-0.789822	-0.227092	0.756344
H3	-0.853953	0.146047	1.077493
H4	-0.633092	0.366908	1.038542
H5	-1.134164	-0.134164	0.559657
H6	-1.336092	-0.336092	1.426181
N1	-0.735693	0.264307	0.754234
N2	-0.927824	0.072176	1.248501
O1	-1.416524	-0.416524	0.753799

**Table S1.** Crystallographic information

<i>P1</i> at 40 GPa			
Lattice Parameters	(Å)	(°)	P (GPa)
	a=4.18483	$\alpha=93.53268$	40
Space Group	b=4.89899	$\beta=114.50651$	
P-1	c=5.05895	$\gamma=111.34557$	
Atom	x	y	z
H1	-0.031562	0.555233	0.277870
H2	0.571216	-0.055934	0.275155
H3	0.477958	0.729867	0.606652
H4	-0.090408	0.735246	0.524810
H5	0.086474	-0.080546	0.304915
H6	0.153359	0.777879	-0.036526
H7	0.569473	0.767817	-0.025791
H8	0.358976	0.556349	0.170563
N1	0.083386	0.755452	0.422716
N2	0.410853	0.760689	0.092884
O1	0.733732	0.737477	0.758691

**Table S2.** Crystallographic information

<i>Cm</i> at 40 GPa				
Lattice Parameters	(Å)	(°)		
	a=5.01170	$\alpha=90.35538$		
	b=5.01170	$\beta=90.35538$		
c=4.42760		$\gamma=49.49192$		
Atom	x	y	z	
H1	1.826421	0.236235	0.950516	
H2	0.654700	0.262343	0.498742	
H3	1.361322	0.975228	0.899360	
H4	-0.059241	0.349228	0.417302	
H9	0.135036	0.135036	0.135697	
H10	0.656185	0.656185	0.763917	
H11	-0.091769	-0.091769	0.119227	
H12	0.667353	0.667353	0.538020	
H13	1.186632	1.186632	0.796638	
H14	-0.405337	0.594663	0.258806	
H15	0.271351	1.271351	0.616189	
H16	-0.237799	0.762201	0.231508	
N1	0.427344	0.427344	0.432090	
N2	0.965679	0.965679	0.951005	
N3	1.287807	1.287807	0.941160	
N4	0.089876	1.089876	0.426344	
O1	0.764723	-0.235277	0.436290	
O2	1.603323	0.603323	0.933290	

**Table S3.** Crystallographic information

<i>Amma</i> at 100 GPa				
Lattice Parameters	(Å)	(°)		
	a=4.10159	$\alpha=90.0000$		
	b=3.93591	$\beta=90.0000$		
c=8.34930		$\gamma=90.0000$		
Atom	x	y	z	
H1	1.249907	0.470293	0.947169	
H2	1.750156	0.518141	0.254183	
H3	2.054955	0.250000	0.606497	
H4	1.961905	0.250000	0.404644	
H5	1.537959	0.250000	0.404637	
H6	1.444750	0.250000	0.606550	
N1	1.749879	0.250000	0.483109	
N2	1.250191	0.750000	1.177484	
O1	1.750188	0.750000	0.661922	

**Table S4.** Crystallographic information

<i>P3m1</i> at 100 GPa			
Lattice Parameters	(Å)	(°)	
	a=3.87096	$\alpha=90.00000$	
	b=3.87096	$\beta=90.00000$	
	c=2.58199	$\gamma=120.00000$	
Atom	x	y	z
H1	0.666667	0.333333	0.742039
H2	0.360936	0.180468	0.238696
N1	0.666667	0.333333	0.357703
O1	0.000000	0.000000	0.000000

**Table S5.** Crystallographic information

<i>Pnna</i> at 300 GPa			
Lattice Parameters	(Å)	(°)	
	a=3.91915	$\alpha=90.00000$	
	b=3.72074	$\beta=90.00000$	
	c=6.71249	$\gamma=90.00000$	
Atom	x	y	z
H1	-0.022939	0.956920	1.147448
H2	-0.462344	0.451029	1.136614
H3	-0.176545	0.762465	0.656199
H4	-0.347914	0.739631	0.443158
N1	-0.398162	0.748495	0.587527
O1	-0.115451	0.250000	0.250000

**Table S6.** Crystallographic information

<i>Pnma</i> at 600 GPa			
Lattice Parameters	(Å)	(°)	
	a=3.96707	$\alpha=90.00000$	
	b=3.22762	$\beta=90.00000$	
	c=5.98678	$\gamma=90.00000$	
Atom	x	y	z
H1	1.156792	0.495967	0.851905
H2	1.677432	0.509783	0.320586
H3	1.984307	0.250000	0.679619
H4	1.862624	0.250000	0.443980
H5	1.496334	0.250000	0.459493
H6	1.154936	0.250000	0.457907
N1	1.681498	0.250000	0.557029
N2	1.300080	0.750000	1.118227
O1	1.968856	0.750000	0.723700

**Table S7.** Crystallographic information

<i>P2<sub>1</sub>/m</i> at 400 GPa			
Lattice Parameters	(Å)	(°)	
	a=5.70349	$\alpha=90.00000$	
	b=3.52038	$\beta=97.90412$	
	c=2.24096	$\gamma=90.00000$	
Atom	x	y	z
H1	0.319669	-0.511019	0.302069
H2	0.848876	-0.006609	0.181909
H9	0.410249	-0.750000	0.897519
H10	0.557144	-0.750000	0.339177
H13	0.924471	-0.250000	0.716142
H14	1.111486	-0.250000	0.278069
N1	0.392262	-0.750000	0.472131
N3	0.941276	-0.250000	0.286887
O1	0.279157	-0.250000	-0.079104

**Table S8.** Crystallographic information

<i>P2<sub>1</sub>/c</i> at 600 GPa			
Lattice Parameters	(Å)	(°)	
	a=10.83316	$\alpha=90.00000$	
	b=3.37127	$\beta=99.57314$	
	c=2.15195	$\gamma=90.00000$	
Atom	x	y	z
H1	0.153288	0.476515	0.311418
H2	0.425244	0.015799	0.174453
H3	0.339784	1.008925	0.701268
H4	0.074128	0.482431	0.825957
H9	0.202084	0.218927	0.923936
H10	0.276246	0.274393	0.359065
H13	0.462693	0.770254	0.709074
H14	0.561760	0.763523	0.302229
N1	0.192773	0.239126	0.489587
N3	0.473403	0.766567	0.266675
O1	0.143322	0.734427	0.909052

**Table S9.** Crystallographic information

AHH-I at 1 GPa			
Lattice Parameters	(Å)	(°)	
	a=5.36458	$\alpha=90.000000$	
	b=7.89413	$\beta=92.571178$	
c=8.08543	$\gamma=90.000000$		
Atom	x	y	z
H1	0.386473	0.533238	0.826563
H2	0.924102	0.463913	0.171713
H3	0.923993	0.833118	-0.048053
H4	0.622616	0.859833	-0.085704
H5	0.724078	0.725106	0.056162
H6	0.245945	0.587084	0.997357
H7	0.260117	0.803133	0.794102
H8	0.264519	1.004506	0.841259
N1	0.235628	0.596894	0.870305
N2	0.243294	0.158007	0.992918
O1	0.285347	0.920860	0.747851

**Table S10.** Crystallographic information

AHH-II at 10 GPa			
Lattice Parameters	(Å)	(°)	
	a=3.16423	$\alpha=90.000000$	
	b=8.84224	$\beta=93.33907$	
c=8.33336	$\gamma=90.000000$		
Atom	x	y	z
H1	0.761617	0.027000	0.367719
H2	0.775042	0.126474	0.537683
H3	0.383072	0.145450	0.401705
H4	0.733247	0.875884	0.024040
H5	0.722634	0.777506	0.855109
H6	0.338617	0.894919	0.889162
H7	0.147588	0.781785	0.182418
H8	0.168637	0.966279	0.187997
N1	0.703285	0.131017	0.415613
N2	0.658850	0.881119	0.902831
O1	0.037847	0.874446	0.240317

**Table S11.** Crystallographic information